PAPER • OPEN ACCESS

Multiple ion temperature gradient driven modes in transport barriers

OPEN ACCESS
IOP Publishing | International Atomic Energy Agency
Nuclear Fusion
Nucl. Fusion **57** (2017) 046019 (14pp)
https://doi.org/10.1088/1741-4326/aa5d02

Multiple ion temperature gradient driven modes in transport barriers

M.K. Han[1,2], Zheng-Xiong Wang[1], J.Q. Dong[2,3] and Huarong Du[1]

[1] Key Laboratory of Materials Modification by Laser, Ion and Electron Beams (Ministry of Education), School of Physics and Optoelectronic Technology, Dalian University of Technology, Dalian 116024, People's Republic of China
[2] Southwestern Institute of Physics, Chengdu 610041, People's Republic of China
[3] Institute for Fusion Theory and Simulation, Zhejiang University, Hangzhou 310027, People's Republic of China

E-mail: zxwang@dlut.edu.cn

Received 9 November 2016, revised 11 January 2017
Accepted for publication 27 January 2017
Published 6 March 2017

Abstract

The ion temperature gradient (ITG) modes in transport barriers (TBs) of tokamak plasmas are numerically studied with a code solving gyrokinetic integral eigenvalue equations in toroidal configurations. It is found that multiple ITG modes with conventional and unconventional ballooning mode structures can be excited simultaneously in TBs with steep gradients of ion temperature and density. The characteristics of the modes, including the dependence of the mode frequencies, growth rate and structure on plasma parameters, are systematically investigated. Unconventional modes with large mode-number l (where l denotes a certain parity and peak number in ballooning space) dominate in the large $k_\theta\rho_s$ region ($k_\theta\rho_s \geqslant 1.2$), while the conventional mode with $l = 0$ dominates in the medium $k_\theta\rho_s$ region ($0.4 \leqslant k_\theta\rho_s < 1.2$), and unconventional modes with small mode-number l dominate in the small $k_\theta\rho_s$ region ($k_\theta\rho_s < 0.4$). Thus, the $k_\theta\rho_s$ spectra of these conventional and unconventional modes at steep gradients are qualitatively different from those of the conventional ITG modes at small or medium gradients, in which the growth rate of the only ITG mode with $l = 0$ reaches maximum at the medium value $k_\theta\rho_s = 0.6$. Through scanning ion temperature gradient $\varepsilon_{T\mathrm{i}}$ and density gradient ε_n separately, it is proven that the synergetic effect of $\varepsilon_{T\mathrm{i}}$ and ε_n, rather than $\varepsilon_{T\mathrm{i}}$ alone, drives the unconventional ITG modes in TBs. Moreover, it is found that the critical value of ε_n for driving the unconventional ITG modes with large l number increases with increasing $k_\theta\rho_s$. In addition, the effects of magnetic shear on conventional and unconventional ITG modes in the high confinement regime (H-mode) are analyzed in detail, and compared with equivalent effects on conventional modes in the low and intermediate gradient regimes (L- and I- modes). Finally, the effects of the poloidal wave number and gradients of ion temperature and density on radial transport are analyzed based on quasi-linear mixing length estimations.

Keywords: ion temperature gradient instability, transport barriers, turbulence

(Some figures may appear in colour only in the online journal)

1. Introduction

Transport barriers (TBs) with steep density and/or temperature gradients are desirable for magnetic fusion plasmas, since confinement is significantly improved in such barriers. Great efforts have been made, and significant progress has been achieved, in understanding the formation mechanisms and advancing transport barrier performance. On the other hand, despite growing efforts in the study of transport in TBs, there is no consensus to date on quite a few issues, such as the mechanism for residual electron heat transport in TBs. It is well accepted that anomalous cross-field particle, momentum, and energy transport is associated with the presence of small scale turbulence in tokamaks [1–5]. In addition, ion temperature gradient (ITG) instabilities have been widely considered as a major candidate to explain ion-scale turbulent transports and, therefore, intensively studied experimentally and theoretically. However, most previous studies have focused on modes in core plasmas of low or medium temperature and density gradients. For example, Dong *et al* derived an integral equation including magnetic curvature and gradient drift motions of ions, and linear mode coupling caused by spatial inhomogeneity in toroidal magnetic configurations [5]. Possible correlations between ITG modes and some experimental results were discussed at medium gradients. Moreover, Li *et al* observed ITG modes of ballooning structures with even or odd parity at medium gradients [6]. It was found that the behaviors of modes with even and odd symmetries are quite different, when wave–particle interactions are considered.

In experiment, high confinement (H-mode) plasmas are characterized by steep gradients of both temperature and density, and edge transport barriers (ETBs) are observed in so called pedestals at plasma edge. In addition, regions of steep temperature and density gradients also exist, and so called internal transport barriers (ITBs) are observed in core plasmas [7–10]. Furthermore, a new improved energy confinement mode (I-mode) in a stationary edge pedestal has been observed recently on some tokamak devices, including Alcator C-Mod [11, 12] and DIII-D [13]. An I-mode discharge is characterized by a steep temperature gradient, comparable to those in H-mode, while the density gradient remains identical to those in low confinement mode (L-mode). It is worth pointing out that decoupling between particle and energy transports, as observed in the I-mode discharges, are common even in ITB experiments.

The steep gradients in TBs can drive a variety of instabilities, including, of course, the ITG instability [3, 13]. Therefore, a crucial problem encountered in tokamak research is better understanding of the properties of instabilities and mechanisms for favorable confinement in TBs [14–16]. Recently, Fulton *et al* found that in the pedestal region of the DIII-D tokamak the electrostatic instability exhibited an unusual mode structure, which peaked at the poloidal angle $\theta = \pm\pi/2$. They also demonstrated that such unconventional mode structure was due to the steep pressure gradients in pedestals instead of the specific magnetic geometry of DIII-D [13]. Through a pressure scan in the pedestal region of DIII-D, E. Wang *et al* found that even though micro-tearing mode might be excited [15], the electrostatic ITG mode could still be dominant in some parameter regimes at the top of the pedestal. Xu *et al* found that in comparison with ELMy H-mode in pedestals, I-mode had a lower pedestal pressure and current due to lack of a particle barrier, exhibiting ELM-free operating properties [16], and the particle and energy transport channels were clearly decoupled. For this reason, I-mode is a valuable operation regime for exploring the underlying physical mechanisms of transport as well as for the transition to H-modes [12].

Actually, a number of ITG modes with unconventional ballooning mode structures, characterized by peaking at arbitrary poloidal positions, have been observed in simulations [1, 2, 13, 17, 18]. These were considered as possible candidates to explain the transport in TBs. Singh *et al* studied the unconventional eigenmodes with nonzero ballooning angle, which have an important influence on the parity of the associated heat flux [19]. More recently, Xie *et al* found that at steep gradients the most unstable mode might not be the usual so called ground eigenstate [17, 21], since the most unstable mode has unconventional ballooning structure. Such results may account for the better confinement in H-mode. Rafiq *et al* found that the unconventional modes can be affected by geometrical effects in 3D stellarator geometry [18]. Although these ITG modes of unconventional ballooning structures were numerically discovered recently, their physical properties are far from well investigated. For instance, the basic characteristics and exciting conditions of the modes have not been obtained and described completely. In addition, individual roles played by the ITG and density gradient in exciting such ITG modes have not been discussed in detail. In particular, the dominant plasma parameter regimes, where multiple unstable ITG eigenmodes of both conventional and unconventional ballooning structures intrinsically appear simultaneously, have not been identified.

In the present work, we investigate the characteristics of the ITG modes in TBs of tokamaks, by using the updated toroidal gyrokinetic code HD7. It is found that multiple unstable ITG modes with conventional and unconventional ballooning mode structures coexist in TBs. Here, the unconventional ballooning mode structures mean that there are one or multiple peaks located off from the mid-plane at the lower field side, while the conventional one has one peak in the mid-plane at the lower field side. The spectra of these conventional and unconventional ITG modes at steep gradients, which are qualitatively different from those of conventional ITG modes, are investigated systematically. The effects of ITGs on both conventional and unconventional ITG modes are studied in detail. Moreover, the key role of density gradient in exciting unconventional ITG modes is explored. The effects of magnetic shear on both conventional and unconventional ITG modes at steep gradients are discussed in detail and compared with those on conventional ITG modes at small/medium gradients. Finally, rough estimations on turbulent transport induced by both conventional and unconventional ITG instabilities are presented, based on the quasi-linear radial mixing length approximation. Results reported in this work provide a new perspective and may help in understanding the complicated transport in TBs.

The remainder of this paper is organized as follows. Section 2 details the integral eigenmode equation and physical model. The numerical results are analyzed in section 3. Finally, the summary and discussion of the results are given in section 4.

2. Integral eigenmode equation and physical model

The gyrokinetic integral equation, widely applied in studies of low-frequency electrostatic micro-instabilities in inhomogeneous axisymmetric toroidal plasmas, is derived briefly in this section. In this equation, the ion toroidal drifts induced by the magnetic curvature and magnetic gradient $\omega_{\rm D}(v_\perp^2, v_{//}^2, \theta)$, the ion transit motion $k_{//}v_{//}$, and full finite Larmor radius (FLR) effects are all retained, while ion magnetic trapping is neglected. In addition, the electrons are assumed to be adiabatic, and trapped electrons are neglected. The ballooning representation is employed so that the linear mode coupling due to the toroidal magnetic configuration is taken into account. The $s-\alpha$ equilibrium model with circular flux surfaces is adopted.

The adiabatic electron response is expressed as

$$\tilde{n}_{\rm e} = \frac{n_{0\rm e}e}{T_{\rm e}}\tilde{\phi}. \tag{1}$$

The ion response is given by

$$\tilde{n}_{\rm i} = -\frac{n_{0\rm i}e}{T_{\rm i}}\tilde{\phi} + \int {\rm d}^3 v J_0(\alpha_{\rm i}) h, \tag{2}$$

where $T_{\rm i}$ and $T_{\rm e}$ are the temperature of the ions and electrons respectively, $\hat{v}_\perp = v_\perp/v_{\rm Ti}$, $\hat{v}_{//} = v_{//}/v_{\rm Ti}$, $v_{\rm Ti} = (2T_{\rm i}/m_{\rm i})^{1/2}$, $\alpha_{\rm i} = k_\perp v_{\rm Ti}/\Omega_{\rm i}$. $\Omega_{\rm i} = eB/m_{\rm i}c$ is the ion gyro-frequency, $J_0(\alpha_{\rm i})$ is the zeroth-order Bessel function. The non-adiabatic response h has to be determined by solving the gyro-kinetic equation [22],

$$i\frac{v_{//}}{qR}\frac{\partial}{\partial\theta}h + (\omega-\omega_{\rm D})h = (\omega-\omega_{*T})J_0(\alpha_{\rm i})F_{\rm M}\frac{en_{\rm i0}}{T_{\rm i}}\widehat{\phi}(\theta), \tag{3}$$

with

$$\omega_{*T} = -\frac{\omega_{*\rm e}}{\tau_{\rm e}}\left[1+\eta_{\rm i}\left(\hat{v}_\perp^2+\hat{v}_{//}^2-\frac{3}{2}\right)\right],$$

$$\omega_{\rm D} = \frac{2\varepsilon_n\omega_{*\rm e}}{\tau_{\rm e}}(\cos\theta+\hat{s}\theta\sin\theta)\left(\frac{\hat{v}_\perp^2}{2}+\hat{v}_{//}^2\right),$$

where $\widehat{\phi} = e\tilde{\phi}/T_{\rm i}$, and the subscripts 'i' and 'e' stand for ions and electrons respectively. $F_{\rm M} = (\pi v_{T\rm i}^2)^{-3/2}\exp(-\hat{v}_\perp^2-\hat{v}_{//}^2)$ is the Maxwellian distribution function, $\omega_{\rm D}$ represents ∇B and curvature drift frequency in a circular flux surface equilibrium, and $\omega_{*\rm e} = ck_\theta T_{\rm e}/eBL_n$ is the electron diamagnetic drift frequency. $L_{T\rm i} = -(d\ln T_{\rm i}/dr)^{-1}$ and $L_n = -(d\ln n/dr)^{-1}$ are the scale lengths of the ITG and density gradient respectively. $\varepsilon_n = L_n/R$ and $\varepsilon_{T\rm i} = L_{T\rm i}/R$, where R is the major radius of the torus, are used as dimensionless primary variables, representing the density and ITGs respectively. $\eta_{\rm i} = L_n/L_{T\rm i}$ is the ratio of the density gradient to the ITG and considered as a secondary variable. We investigate the effects of ion density and temperature gradients separately, by scanning ε_n and $\varepsilon_{T\rm i}$. The following ballooning representation has been used in deriving equation (3),

$$\tilde{f}_s(r,\theta,\zeta) = \sum_{m=-\infty}^{\infty} e^{im\theta}\int_{-\infty}^{\infty} e^{-im\theta'}\cdot e^{-i(\zeta-q\theta')-i\omega t}\tilde{f}_n(\theta'){\rm d}\theta', \tag{4}$$

where θ and ζ are the extended poloidal and the toroidal angles respectively. The solution of equation (3) with the boundary condition $h=0$ as $\theta\to\pm\infty$ [20, 23] can be written as

$$h_+ = -i\int_{-\infty}^{\theta} d\theta' \frac{qR}{|v_{//}|}e^{i\sigma_{\rm i}(\theta,\theta')}\cdot(\omega-\omega_{*T})F_{\rm M}\frac{n_{0\rm i}e}{T_{\rm i}}\widehat{\phi}(\theta),$$
$$h_- = -i\int_{\theta}^{\infty} d\theta' \frac{qR}{|v_{//}|}e^{-i\sigma_{\rm i}(\theta,\theta')}\cdot(\omega-\omega_{*T})F_{\rm M}\frac{n_{0\rm i}e}{T_{\rm i}}\widehat{\phi}(\theta), \tag{5}$$

where

$$\sigma_{\rm i} = \sigma_{\rm i}(\theta) = \int_{\theta_0}^{\theta} d\theta' \frac{qR}{|v_{//}|}(\omega-\omega_{\rm D}(\theta')),$$
$$\sigma_{\rm i}' = \sigma_{\rm i}(\theta') = \int_{\theta_0}^{\theta'} d\theta'' \frac{qR}{|v_{//}|}(\omega-\omega_{\rm D}(\theta'')).$$

From the quasineutrality condition $\tilde{n}_{\rm e} = \tilde{n}_{\rm i}$, we obtain,

$$\left(\frac{1}{\tau_{\rm e}}+1\right)\widehat{\phi}(\theta) = \int {\rm d}^3 v J_0(\alpha_{\rm i})(h_+ + h_-). \tag{6}$$

Through some mathematical manipulations, equation (6) is reduced to the following integral eigenvalue equation

$$(\tau_{\rm e}+1)\widehat{\phi}(\theta) = \int_{-\infty}^{+\infty} d\theta' K(\theta,\theta')\widehat{\phi}(\theta'), \tag{7}$$

$$K(\theta,\theta') = -i\tau_{\rm e}\int_0^{\infty} 2\pi v_\perp dv_\perp \int_0^{\infty} dv_{//}\frac{qR}{|v_{//}|}e^{i{\rm sgn}(\theta-\theta')(\sigma_{\rm i}(\theta)-\sigma_{\rm i}(\theta'))}$$
$$\cdot(\omega-\omega_{*T})J_0(\alpha_{\rm i})J_0(\alpha_{\rm i}')F_{\rm M}. \tag{8}$$

After the integration over $v_\perp$ in equation (8), we change the integration over $v_{//}$ to integration over τ, by introducing

$$\tau = \frac{qR|\theta-\theta'|}{v_{//}v_{\rm Ti}}. \tag{9}$$

We also use the dimensionless variables $k = \widehat{S}(r_0)k_\theta\theta = \widehat{S}(r_0)\frac{m}{r_0}\theta$ and $k' = \widehat{S}(r_0)k_\theta\theta' = \widehat{S}(r_0)\frac{m}{r_0}\theta'$, which are the Fourier transform of the radial variable $x = r-r_0$ (r_0 being defined by $q(r_0) = \frac{m}{n}$) in the toroidal model. Through the conversion from θ to k, the integral equations (7) and (8) can be written as [5]

$$(1+\tau_{\rm e})\widehat{\phi}(k) = \int_{-\infty}^{+\infty}\frac{dk'}{\sqrt{2\pi}}K(k,k')\widehat{\phi}(k'), \tag{10}$$

with

$$K(k,k') = -\mathrm{i}\int_{-\infty}^{0}\omega_{*\mathrm{e}}\mathrm{d}\tau\frac{\sqrt{2}\,\mathrm{e}^{-\mathrm{i}\omega\tau}}{\sqrt{a}(1+a)\sqrt{\lambda}}\mathrm{e}^{-\frac{(k-k')^2}{4\lambda}}\Gamma_0(k_\perp,k'_\perp)$$
$$\times\left[\frac{\omega\tau_\mathrm{e}}{\omega_{*\mathrm{e}}}+1-\frac{3\eta_\mathrm{i}}{2}+\frac{2\eta_\mathrm{i}}{(1+a)}\left(1-\frac{k_\perp^2+k'^2_\perp}{2(1+a)\tau_\mathrm{e}}+\frac{k_\perp k'_\perp}{(1+a)\tau_\mathrm{e}}\frac{I_1}{I_0}\right)+\frac{\eta_\mathrm{i}(k-k')}{4a\lambda}\right], \tag{11}$$

$$\lambda = \frac{\tau^2}{\tau_\mathrm{e}a}\left(\frac{\hat{s}}{q}\varepsilon_n\right)^2\omega_{*\mathrm{e}}^2, \tag{12}$$

$$\Gamma_0 = I_0\left(\frac{k_\perp k'_\perp}{\tau_\mathrm{e}(1+a)}\right)\mathrm{e}^{-(k_\perp^2+k'^2_\perp)/2\tau_\mathrm{e}(1+a)}, \tag{13}$$

$$k_\perp^2 = k_\theta^2+k^2,\ k'^2_\perp = k_\theta^2+k'^2, \tag{14}$$

$$a = 1+\frac{\mathrm{i}2\varepsilon_n}{\tau_\mathrm{e}}\omega_{*\mathrm{e}}\tau\times\left(\frac{[(\hat{s}+1)(\sin\theta-\sin\theta')-\hat{s}(\theta\cos\theta-\theta'\cos\theta')]}{(\theta-\theta')}\right), \tag{15}$$

$$\theta = \frac{k}{\hat{s}k_\theta},\ \theta' = \frac{k'}{\hat{s}k_\theta}. \tag{16}$$

The radial wave vectors k and k', related to the extended poloidal angle θ and the poloidal wave vector k_θ, are normalized to ρ_s^{-1} with $\rho_s = (2T_\mathrm{e}/m_\mathrm{i})^{1/2}/\Omega_\mathrm{i} = c(2T_\mathrm{e}m_\mathrm{i})^{1/2}/\mathrm{e}B$, and $I_j\,(j=0,1)$ is the modified Bessel function of order j. In addition, all the standard symbols have their conventional meanings—for instance, q is safety factor, $\hat{s} = r\mathrm{d}q/q\mathrm{d}r$ is magnetic shear, and $\tau_\mathrm{e} = T_\mathrm{e}/T_\mathrm{i}$ is the ratio of electron temperature to ion temperature.

The above equation is similar to those used by Dong *et al* [5], Romanelli [20], and H. Sugama [23]. Since the ballooning representation is employed for the toroidal coupling of ITG modes, the θ-variation is dominant. It has to be mentioned that we have neglected effects of finite ballooning angle and assumed $\theta_0 = 0$ in this work. Such effects will be considered in future works with the upgraded code HD7. Thus, the original 2D problem is approximated with one of calculating the mode structure along the magnetic field lines [23] to the lowest order of $1/n$, with n being the toroidal mode number. Moreover, the ρ_* expansion used in the gyrokinetic equation derivation is validated because the ratio of the ion Larmor radius to the gradient scale lengths is assumed to be small enough ($\rho_* \ll 1$).

For the numerical results presented in this work, we updated the gyrokinetic code HD7 to solve the linear gyrokinetic integral equation for both symmetric (even-parity or odd-parity) and asymmetric eigenmode structures. The reliability of the unconventional ITG mode solutions of HD7 code is attested by the GTC code [17]. HD7 code has been extensively applied in studies of micro-instabilities and turbulence, such as impurity effects [22, 25], trapped electron mode [26], electron temperature gradient mode [27], velocity shear [28], anisotropy of ITG [29], electromagnetic perturbations (Alfvén modes driven by ITG [30], kinetic ballooning mode [31], kinetic shear Alfvén modes [32]), elongated cross section [33], and reversed field pinch configuration [34]. Recently, the results of HD7 code have provided appreciable support for experimental observations at the HL-2A tokamak [35]. In addition, HD7 code has been benchmarked with other numerical simulation codes, such as GYRO, GEM, GS2, GTC, GT3D, and FULL [15, 36].

3. Numerical results

It should be noted that the ratio of density gradient to temperature gradient is considered as a secondary variable in this work. In order to identify individual roles of the ion temperature and density gradients separately, the dimensionless variable $\varepsilon_{T\mathrm{i}}$, representing ITG, is introduced into the HD7 code as a primary parameter for the first time. The parameter ε_n in this work may be considered as representing the density gradient in internal/edge transport barriers, according to [12, 17]. In particular, if $\varepsilon_{T\mathrm{i}}$ and ε_n are both small, these parameters correspond to the gradients of H-mode in pedestals. On the other hand, the parameters correspond to the gradients in the edge of I-mode if the $\varepsilon_{T\mathrm{i}}$ is small but ε_n is medium. If both $\varepsilon_{T\mathrm{i}}$ and ε_n are medium, the parameters correspond to the gradients in L-mode plasmas. Parameters used in this work are: $k_\theta\rho_s = 0.6$, $q = 3$, $\hat{s} = 1.6$, $\varepsilon_n = 0.044$, $\varepsilon_{T\mathrm{i}} = 0.007$ and $\tau_\mathrm{e} = 1$ unless otherwise stated. It should be noted that both the growth rate and real frequency are usually normalized to $\omega_{*\mathrm{e}}$, while the growth rate and real frequency in figures 3–6 are normalized to $\omega_{*\mathrm{e}}(k_\theta\rho_s)^{-1}$, because the electron diamagnetic drift frequency is proportional to $k_\theta\rho_s$.

3.1. Observation of multiple ITG modes

Since the ballooning representation is employed for toroidal mode coupling, the θ-variation is a dominant feature of the mode structures along the magnetic field lines [24]. Multiple ITG modes with conventional and unconventional ballooning mode structures are found unstable—in contrast to regions with low or medium gradients, where only one mode with conventional ballooning mode structure is unstable. One example is given in figure 1, where the eigenmodes with distinguishable structures in the ballooning space are presented. The parameters for the results are $k_\theta\rho_s = 0.6$, $\varepsilon_n = 0.044$, $\varepsilon_{T\mathrm{i}} = 0.007$, $\hat{s} = 1.6$, $q = 3$ and $\tau_\mathrm{e} = 1$. Each mode is assigned a mode-number l in accordance with its parity and number of peaks for convenience of description. For example, the mode with even parity (symmetric with respect to the middle plane) and one peak is designated $l = 0$, while the mode with odd parity (anti-symmetric with respect to the middle plane) and two peaks is called $l = 1$, and so on. It is very clear that an even l corresponds to a mode with even parity, while an odd l represents a mode with odd parity. In addition, for modes with the same parity, the higher l is, the more peaks the mode structure has. In this sense, the number l may be considered as a harmonic number. For instance, eigenfunctions $\widehat{\phi}(\theta)$ in figures 1(a) and (b) represent the lower-order harmonics, and those in figures 1(c)–(f) represent the higher-order harmonics.

The width of the eigenfunction in the ballooning space is an important parameter for physics analysis and mixing length estimation of quasi-linear turbulent transport coefficients. The

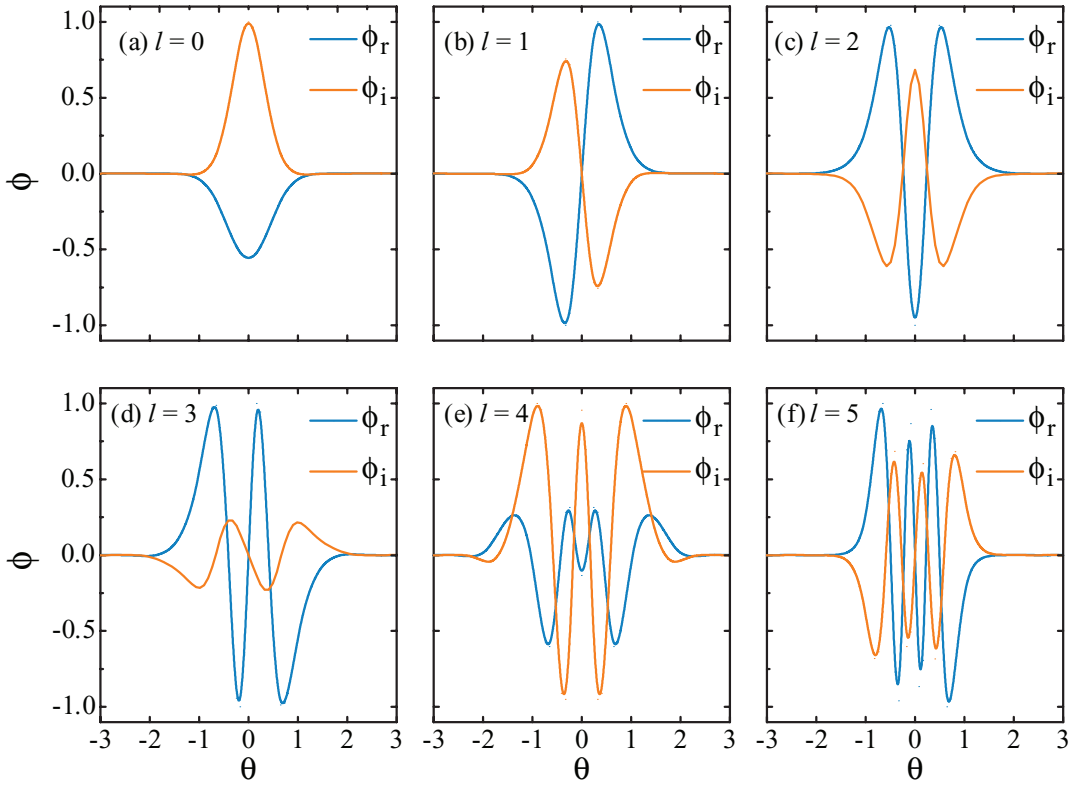

Figure 1. Typical eigenfunction $\widehat{\phi}(\theta)$ of unconventional ITG modes with $l = 0$–5 and $k_\theta\rho_s = 0.6$ at steep gradients for $\varepsilon_n = 0.044$, $\varepsilon_{Ti} = 0.007$. The other parameters are $\hat{s} = 1.6$, $q = 3$ and $\tau = 1$. Blue lines represent the real part; orange lines the imaginary part.

following formula is applied to estimate the average width of the eigenfunction in ballooning space:

$$\langle\theta^2\rangle^{1/2} = \sqrt{\frac{\int\theta^2\left|\widehat{\phi}(\theta)\right|^2 \mathrm{d}\theta}{\int\left|\widehat{\phi}(\theta)\right|^2 \mathrm{d}\theta}}. \tag{17}$$

It is found in figure 1 that the widths of the eigenfunctions in ballooning space gradually broaden with increasing mode-number l. For instance, the width changes from $\langle\theta^2\rangle^{1/2} = 0.25248$ for $l = 0$ to $\langle\theta^2\rangle^{1/2} = 0.9282$ for $l = 5$. It is worth pointing out that, as shown in figure 2, the eigenfunctions given in figure 1 gain more fine structure at the boundary for increasing $k_\theta\rho_s$, although the outlines are almost unchanged. This observation suggests that higher resolution is required in order to obtain these modes. In addition, it is interesting to note that, for the modes with mode-number $l = 0$ and $l = 2$, figure 2 depicts that the increase of $k_\theta\rho_s$ tends to enlarge the peak-number of the eigenfunctions of both conventional and unconventional ITG modes in ballooning space, and broaden the eigenfunctions. For example, the width of the eigenfunction for the mode with $l = 0$ increases from $\langle\theta^2\rangle^{1/2} = 0.183\,24$ for $k_\theta\rho_s = 1.09$ to $\langle\theta^2\rangle^{1/2} = 0.2861$ for $k_\theta\rho_s = 1.48$, and for the mode with $l = 2$ the width increases from $\langle\theta^2\rangle^{1/2} = 0.445\,49$ for $k_\theta\rho_s = 0.81$ to $\langle\theta^2\rangle^{1/2} = 0.656\,78$ for $k_\theta\rho_s = 1.39$. From the results above, we can see that to understand the properties of the modes at steep ion temperature and density gradients better, more mode characteristics should be explored.

3.2. Wave vector spectra

The normalized growth rate $\gamma k_\theta\rho_s/\omega_{*e}$ and real frequency $\omega_r k_\theta\rho_s/\omega_{*e}$ versus $k_\theta\rho_s$ for ITG modes with different ballooning structures are given in figure 3 for $q = 2, 3$ and 4. Other parameters are the same as in figure 1. It is clearly shown in figures 3(*a*) and (*b*) that at steep gradients, the growth rates of modes with $l = 1, 2, 3$ exceed those of conventional modes in the region of $k_\theta\rho_s < 0.378$. Moreover, the modes with larger mode-number ($l = 4, 5$) become dominant in the region of ε_n, although they are somewhat weaker than the conventional modes in the region of $0.378 < k_\theta\rho_s < 1.2$. For a clear comparison, figures 3(*c*) and (*d*) give $\gamma k_\theta\rho_s/\omega_{*e}$ and $\omega_r k_\theta\rho_s/\omega_{*e}$ versus $k_\theta\rho_s$ for ITG modes with conventional ballooning structures at medium gradients for $\varepsilon_n = 0.6$ and $\varepsilon_{Ti} = 0.1$. In contradiction to cases at steep gradients, at the medium gradients modes with l from 1 to 5 are not excited and the shape of the $k_\theta\rho_s$ spectrum is also quite different from those at the steep gradients. For example, the growth rate of the $l = 0$ mode at steep gradients first increases and then slightly decreases with increasing $k_\theta\rho_s$, but at medium gradients it first increases and then quickly decreases with increasing $k_\theta\rho_s$ after reaching the maximum growth rate. It may be concluded that at steep ion temperature and density gradients, the unconventional modes with large mode-number ($l \geqslant 4$) dominate in the large $k_\theta\rho_s$ region ($k_\theta\rho_s \geqslant 1.2$), the conventional modes ($l = 0$) dominate in the medium $k_\theta\rho_s$ region ($0.4 \leqslant k_\theta\rho_s < 1.2$), and the unconventional modes ($l \neq 0$) are dominant in the small $k_\theta\rho_s$ region ($k_\theta\rho_s < 0.4$). The results above may suggest that the excitation

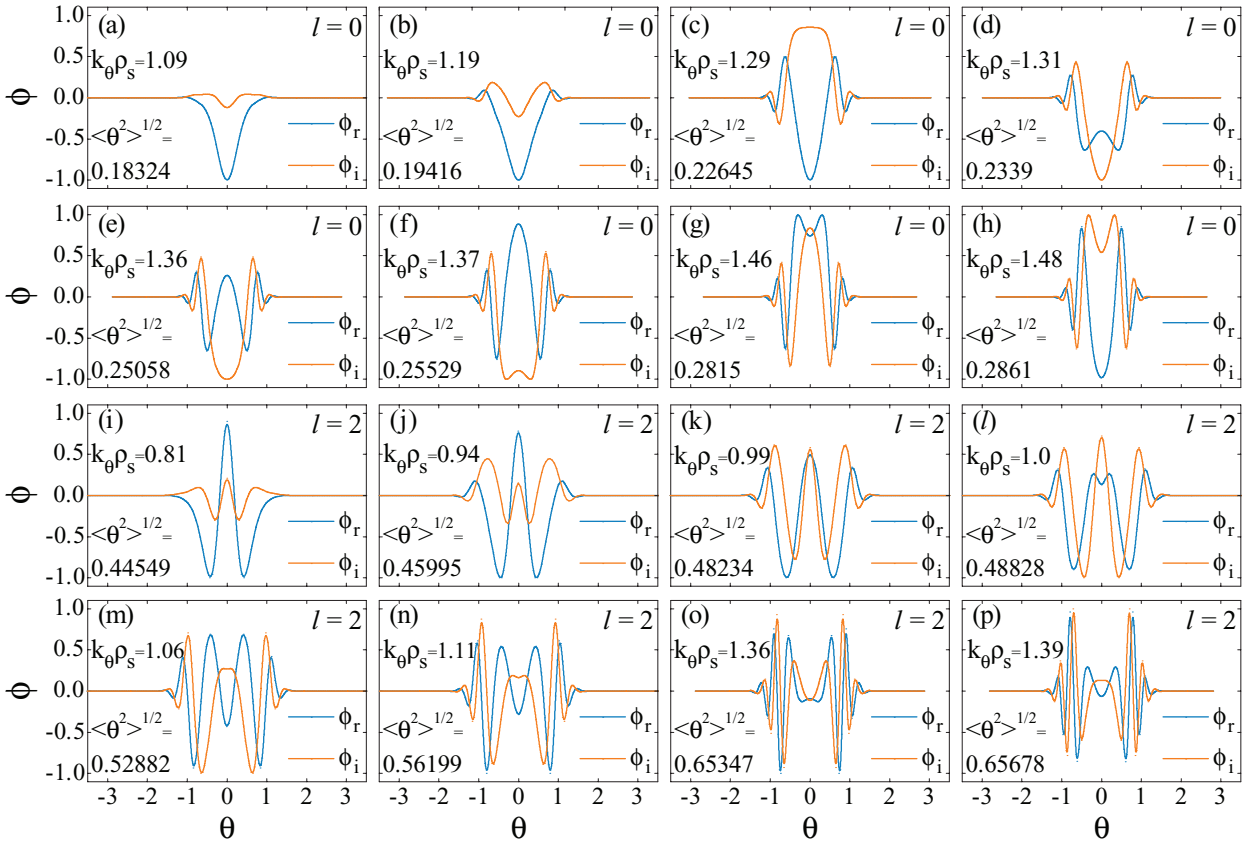

Figure 2. Variation of the eigenfunction structures in ballooning space with increasing $k_\theta\rho_s$ for the ITG modes with $l = 0$ and $l = 2$ in the steep gradients regions. The other parameters are the same as those in figure 1.

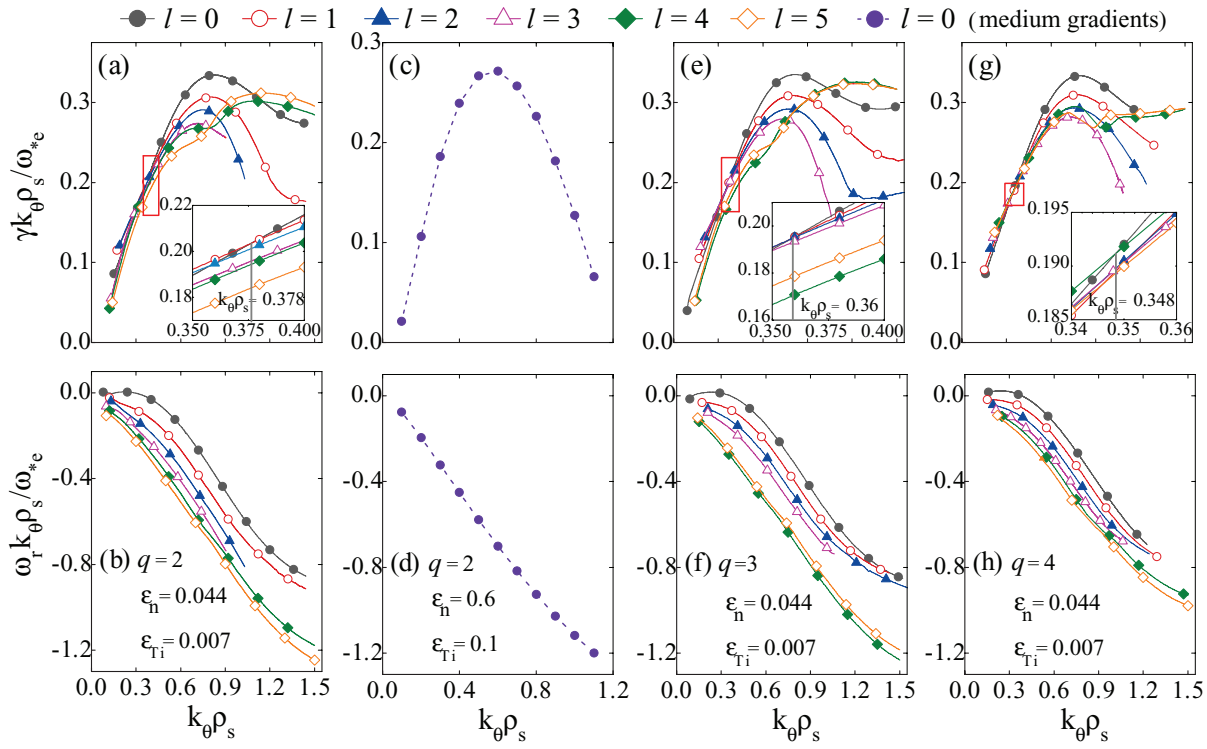

Figure 3. Normalized growth rate $\gamma k_\theta\rho_s/\omega_{*e}$ and real frequency $\omega_r k_\theta\rho_s/\omega_{*e}$ of ITG modes versus $k_\theta\rho_s$ for $q = 2, 3, 4$. (*a*), (*b*) and (*e*)–(*h*) are for ITG modes with $l = 0$–5 at steep gradients of $\varepsilon_n = 0.044$ and $\varepsilon_{Ti} = 0.007$; (*c*) and (*d*) are for conventional ITG mode at medium gradients of $\varepsilon_n = 0.6$ and $\varepsilon_{Ti} = 0.1$. The other parameters are the same as those in figure 1.

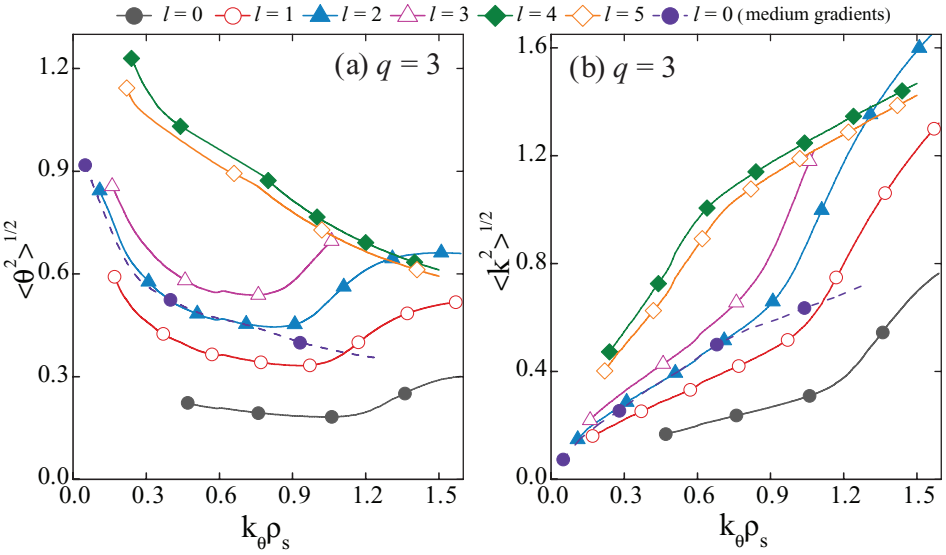

Figure 4. Variation of the width of eigenfunction in the ballooning (a) and k (b) spaces with $k_\theta\rho_s$ for the conventional ITG mode at medium gradients of $\varepsilon_n = 0.6$ and $\varepsilon_{Ti} = 0.1$ and steep gradients of $\varepsilon_n = 0.044$ and $\varepsilon_{Ti} = 0.007$. The other parameters are the same as those in figures 3(e) and (f).

properties of unstable modes at steep gradients (which correspond to the parameters in TBs) are quite different from those at small/medium gradients.

Furthermore, it is found that the safety factor q also plays a significant role in changing the spectra of the ITG modes with different ballooning structures. When the q value increases from 2 to 3, the position of the maximum growth rate of the ITG modes with large mode-number ($l = 4$, 5) shifts from $k_\theta\rho_s \sim 1.1$ to $k_\theta\rho_s \sim 1.21$, while the counterpart with small mode-number (up to $l = 3$) slightly shifts from $k_\theta\rho_s \sim 0.73$ to $k_\theta\rho_s \sim 0.76$. Meanwhile, the dominant region of the modes with large mode-numbers ($l = 4$, 5) becomes larger in the large $k_\theta\rho_s$ region for $q = 3$ in figure 3(e) than that for $q = 2$ in figure 3(a). For $q = 3$, the growth rates of modes with $l = 1$, 2, 3 exceed those of the conventional modes in the region of $k_\theta\rho_s < 0.36$. In comparison, the dominant region of modes with $l = 1$, 2, 3 for $q = 3$ is smaller than that for $q = 2$. For a very large q value ($q = 4$), the growth rates of modes with $l = 1$, 2, 3 exceed those of conventional modes in the region of $k_\theta\rho_s < 0.348$, and their dominant region for $q = 4$ in figure 3(g) is smaller than that for $q = 2$, 3 in figures 3(a) and (e). With increasing $k_\theta\rho_s$, the growth rates of modes with $l = 4$, 5 are comparable to those of other unconventional modes and then become dominant after exceeding them. Besides, figures 3(b), (d) and (f) show that the normalized real frequencies of the modes, propagating in the ion diamagnetic drift direction, slightly decrease with the increase of q, but this tendency is opposite to the cases of the medium gradients in figure 10 of [5]. It can also be seen that the larger the mode-number is, the higher the real frequency. It should be noted that for $q = 2$ in figures 3(a) and (b), the parameters might correspond to the ITBs, while the parameters in figures 3(e)–(h) might correspond to the ETBs.

Different from initial gyrokinetic codes, HD7 is an eigenvalue code that could find not only the most unstable mode but also other multiple unstable modes. Figure 3 can help to account for the 'frequency jump' [13] and 'eigenstate jump' [17], which are shown in some simulations using the initial-value codes. For example, figure 3(g) shows that the most unstable mode in the small and large $k_\theta\rho_s$ regions ($k_\theta\rho_s \leqslant 0.348$ and $1.218 \leqslant k_\theta\rho_s \leqslant 1.5$) is the mode with $l = 4$, but the $l = 0$ mode exceeds others and becomes the dominant mode at steep gradients in the medium $k_\theta\rho_s$ region ($0.348 \leqslant k_\theta\rho_s < 1.218$). Accordingly, such phenomena as 'frequency jump' or 'eigenstate jump' take place at $k_\theta\rho_s = 0.348$ or $k_\theta\rho_s = 1.218$, because one of these modes is the most unstable alternative mode. Consequently, the dominant growth rate, frequency and eigenstate in the system transit from one branch to another at certain critical parameter values when scanning $k_\theta\rho_s$.

Figures 4(a) and (b) depict the variation of the widths of the eigenfunctions in θ and k spaces respectively, as functions of $k_\theta\rho_s$ at the steep (the solid lines) and medium (the dashed lines) gradients of the ion temperature and density. It is shown in figure 4(a) that the widths of the modes with l from 0 to 3 first decrease and then increase with increasing $k_\theta\rho_s$. For the modes with $l = 4$, 5, the widths of the eigenfunctions decrease with the increase of $k_\theta\rho_s$ in the whole $k_\theta\rho_s$ region, though in the region of $k_\theta\rho_s \leqslant 1.0$ the widths are much broader than those of the modes with $l = 0 \sim 3$. It can be seen that although the widths of the conventional modes at medium gradients decrease monotonically with $k_\theta\rho_s$ increasing in the whole $k_\theta\rho_s$ region, they are comparable with that of the mode with $l = 2$ in the small/medium $k_\theta\rho_s$ region ($k_\theta\rho_s \leqslant 0.8$). Meanwhile, figure 4($a$) can also reflect the parallel wavenumber (can be roughly estimated with the ratio of the mode-number to the width of the eigenfunction) which is directly related to the Landau resonance/damping and determines the variation of the linear growth rate. In addition, figure 4(b) shows that at steep ion temperature and density gradients, the eigenfunctions of the unconventional modes in k space

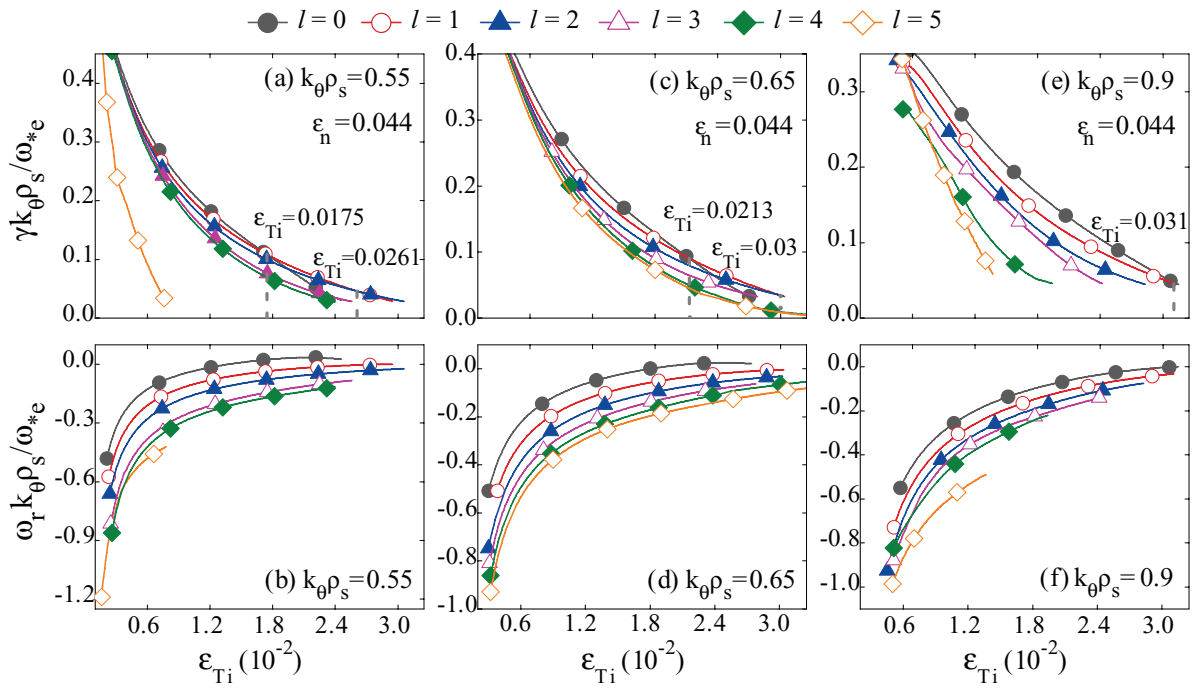

Figure 5. Normalized growth rate and real frequency of the modes with $l = 0$–5 versus ε_{Ti} for $k_\theta\rho_s = 0.55, 0.65, 0.9$. The other parameters are the same as those in figures 3(*e*) and (*f*).

with large numbers $l = 4$, 5 first broaden rapidly in small $k_\theta\rho_s$ region, and then broaden slowly in large $k_\theta\rho_s$ region with the increase of the poloidal wave vector. However, it is quite different for the modes with small mode-numbers ($l = 0$–3), since their eigenfunctions slowly broaden in the small $k_\theta\rho_s$ region and then swiftly broaden in the large $k_\theta\rho_s$ region with increasing $k_\theta\rho_s$, and are even broader than those of the modes with $l = 4$, 5 for $k_\theta\rho_s \geqslant 1.0$. These results may help to understand the behaviors of the spectra given in figure 3. That is, the phenomenon that the unconventional modes with large mode-number are dominant in the large $k_\theta\rho_s$ region can be explained through the FLR effect, since FLR has a stabilizing effect on the modes. The FLR effect is induced through the FLR term J_0 in equation (3). For conventional modes at medium ion temperature and density gradients, figure 4(*b*) illustrates that in the small/medium $k_\theta\rho_s$ region ($k_\theta\rho_s \leqslant 0.8$), the width of the eigenfunction is comparable to those of the unconventional modes with $l = 2$ in k-space. In addition, it is shown that in comparison with the unconventional modes, the width of the eigenfunction of conventional modes increases smoothly in k-space. The results presented above imply that at steep gradients of ion temperature and density, on one hand, the characteristics of the conventional and unconventional ITG modes with different mode-number are different, and that, on the other hand, they are also different from the conventional ITG modes at small or medium gradients. Thus, we see that conventional and unconventional modes obviously make different contributions to turbulent transport in TBs at steep gradients.

More discussions will be dedicated in section 3.6, since the width of the eigenfunction in the ballooning space is an important parameter for physics analysis and mixing length estimation.

3.3. ε_{Ti} variation

Since it is known that both ion temperature and density gradients can provide sufficient free energy to drive instabilities in TBs, it is necessary to distinguish the individual roles of ε_{Ti} and ε_n. In this section, we focus on the role of ITG ε_{Ti}; we go on to study the role of the ion density gradient ε_n in the next section. As analyzed in the previous section, at steep gradients conventional and unconventional ITG modes with different mode-numbers have different spectra in the $k_\theta\rho_s$ space. To compare their physical properties, typical conventional and unconventional ITG modes of $k_\theta\rho_s = 0.5$, 0.65, 0.9 are discussed in this section. A comparison between these modes at medium and steep gradients is also performed.

The normalized growth rate and real frequency as functions of ε_{Ti} are given in figure 5 for $k_\theta\rho_s = 0.5$, 0.65, 0.9, $\hat{s} = 1.6, \varepsilon_n = 0.044, \tau_e = 1$ and $q = 3$. The eigenfunctions $\widehat{\phi}(\theta)$ are similar to the structures in figure 1. It is found that at steep gradients, $\gamma k_\theta \rho_s/\omega_{*e}$ and $\omega_r k_\theta \rho_s/\omega_{*e}$ decrease with increasing ε_{Ti}, indicating that the increase of ITG destabilizes the ITG modes. With increasing ε_{Ti} for $k_\theta\rho_s = 0.55$, as shown in figure 5(*a*), the dominant mode changes from $l = 0$ to $l = 1$ at $\varepsilon_{Ti} = 0.0175$, and then to $l = 2$ at $\varepsilon_{Ti} = 0.0261$. For $k_\theta\rho_s = 0.65$, both critical values for the transition of the dominant modes slightly increase, to $\varepsilon_{Ti} = 0.0213$ and $\varepsilon_{Ti} = 0.03$, as shown in figure 5(*c*). In short, both cases in figures 5(*a*) and (*c*) show that the conventional and unconventional ITG modes with $l = 0$–4 have comparable growth rates across the whole ε_{Ti} regime. Moreover, the mode with $l = 5$ can always be excited in the small ε_{Ti} regime, and also has the same level growth rate as other modes there. Therefore, it is recognized that at a high density gradient (small ε_n value), the roles of unconventional modes with $l > 0$ have to be taken into account

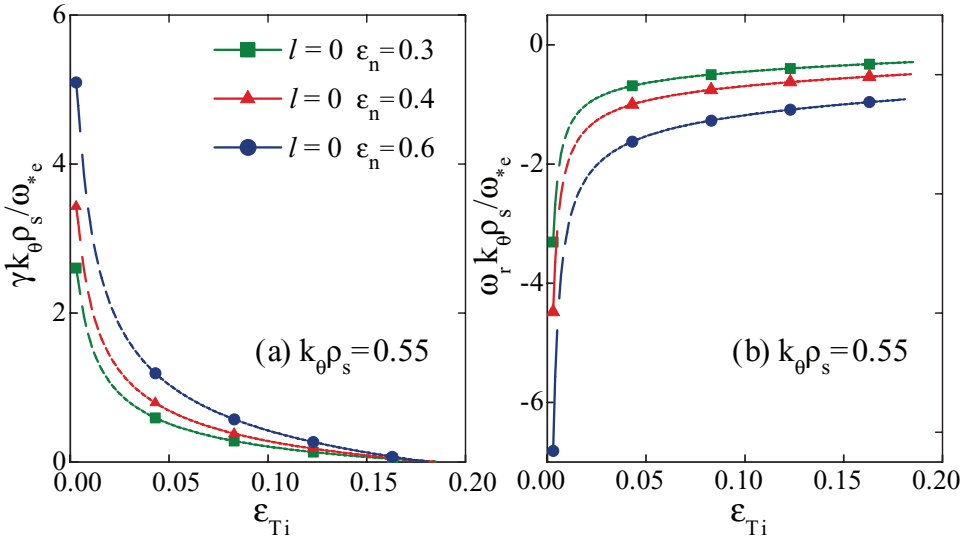

Figure 6. Normalized growth rate and real frequency of the conventional ITG mode versus ε_{Ti} for $k_\theta\rho_s = 0.55$, $\varepsilon_n = 0.3, 0.4, 0.6$ and $q = 3$. The other parameters are the same as those in figures 3(*c*) and (*d*).

across the whole ε_{Ti} regime, and that, in the small ε_{Ti} regime in particular, the $l = 5$ mode can be excited so that the summed role of such unconventional modes significantly exceeds that of the conventional mode.

In experiments, the I-mode is characterized by a large temperature gradient which is comparable to the counterpart of the H-mode and an ordinary density gradient which is comparable to that of the L-mode. Thus, it should be noted that for a steep temperature gradient (here $\varepsilon_{Ti} = 0.0175$), the parameters of the small and medium/large ε_n regimes in figure 5 correspond to the H-mode and I-mode, respectively. The above results suggest that unconventional modes are significantly important parts in the study of the long wave-length ITG modes, and that taking them into account may help in understanding the physical process of transport events in TBs, which will be analyzed based on the quasi-linear mixing length estimation in section 3.6.

For comparison, figure 6 gives the results for small/medium density gradient. Clearly, the conventional ITG modes with $l = 0$ are excited across the whole ε_{Ti} region, but the unconventional ITG modes with $l \neq 0$ are not excited. Besides, figure 6 shows that the growth rates of conventional modes increase with increasing ε_n. Furthermore, since η_i is usually used for measuring ITG, two cases with the same η_i value are compared, in which one is for steep gradients in figure 5(*a*) with $\varepsilon_n = 0.044$ and $\varepsilon_{Ti} = 0.022$, and the other is for medium gradients in figure 6(*a*) for $\varepsilon_n = 0.3$ and $\varepsilon_{Ti} = 0.15$. Obviously, the spectra of unstable modes are completely different and these two cases, indicating that the η_i value alone is not enough to determine the accurate physical process. In other words, the density gradient ε_n is also a key parameter for the excitation of unconventional ITG modes with large mode-numbers, which will be systematically studied in the next section.

3.4. ε_n effect

Here we focus on the dependence of excitation of unconventional ITG modes on density gradient ε_n. Assuming the inverse aspect ratio ($\varepsilon = r/R$) $\varepsilon = 3$, both the growth rate and real frequency are normalized to $3\varepsilon_n\omega_{*e}/k_\theta\rho_s$, to remove the influence of normalization in the comparison. The effects of ε_n on the unconventional ITG modes are shown in figure 7. It is observed in figures 7(*a*) and (*c*) that with increasing ε_n, in general, the growth rates of the modes with $l = 0$–3 first increase and then decrease in the small/medium $k_\theta\rho_s$ region. This observation recalls the effect shown in [37], where the growth rates first increase and then decrease. For a very steep density gradient in the cases of $k_\theta\rho_s = 0.6$, 0.8 the modes with $l = 4$, 5 can also be excited and have comparable growth rates to the modes with $l = 0$–3. With increasing ε_n, the growth rates of the $l = 4$, 5 modes gradually become smaller than those of the $l = 0$–3 modes. Then the $l = 4$, 5 modes disappear at a critical value of ε_n. It is observed that this critical value of ε_n increases with increasing $k_\theta\rho_s$, for example, 0.0581 for $k_\theta\rho_s = 0.6$ and 0.0589 for $k_\theta\rho_s = 0.8$. For a large $k_\theta\rho_s$ value ($k_\theta\rho_s = 1.2$), as shown in figure 7(*e*), the $l = 4$, 5 modes are dominant over a large part of the ε_n regime, whereas the $l = 0$ mode is significantly stabilized by increasing ε_n. It is concluded that for a small/medium $k_\theta\rho_s$ value, a very strong density gradient (small ε_n value) is needed to excite the $l = 4$, 5 modes, whereas for a large $k_\theta\rho_s$ value the $l = 4$, 5 modes are easily excited and dominant over a wide ε_n regime. Besides, the parameters used and the results found here are similar to the stability diagram depicted in figure 1 of [37], which is found using fluid theory. It should be pointed out that this picture will change drastically if trapped electrons or electromagnetic effects are taken into account.

The discussions in figures 6–8 reveal that it is the synergistic effects of ion temperature and density gradients that drive the unconventional ITG modes. In TBs with steep gradients of ion temperature and density, the turbulent transport induced by such unconventional ITG modes should be paid more attention, especially in the large $k_\theta\rho_s$ regime where the modes with higher l numbers are dominantly unstable. The role of such unconventional ITG modes in the transition of different confinement states should be taken into account as well. It is necessary to note that trapped electron modes can

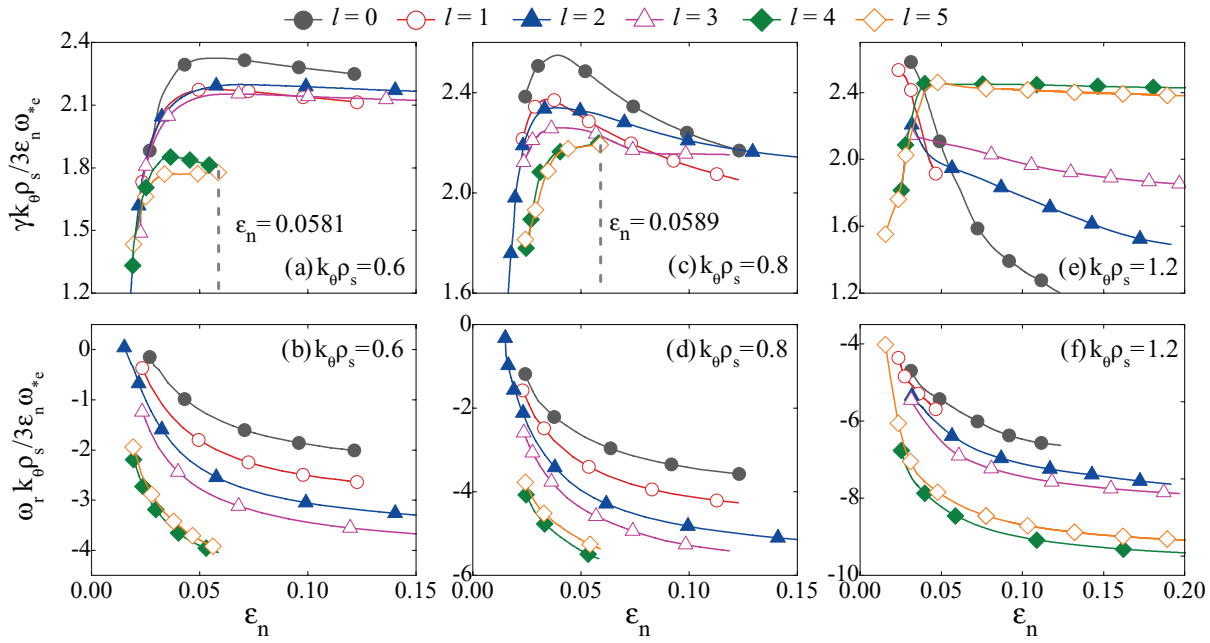

Figure 7. Normalized growth rate and real frequency of the modes with $l = 0$–5 versus ε_n for $k_\theta\rho_s = 0.6, 0.8, 1.2$. The other parameters are the same as those in figures 3(*e*) and (*f*).

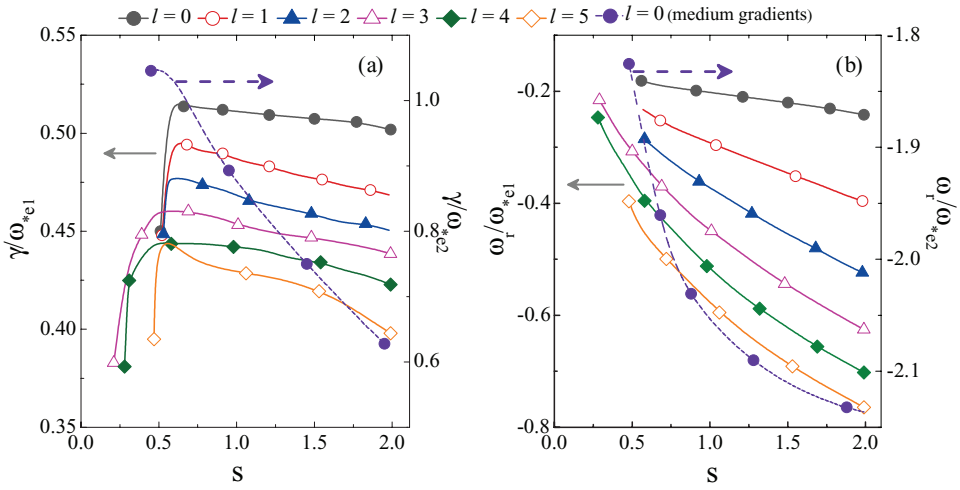

Figure 8. Normalized growth rate and real frequency of the conventional and unconventional ITG modes versus $\hat{s}$ for $k_\theta\rho_s = 0.6$ and $q = 3$. The growth rate and real frequency of the modes in the steep gradient regime and those in the medium gradient regime are normalized to ω_{*e1} and ω_{*e2} respectively. The other parameters are the same as those in figures 3(*c*)–(*f*).

be driven by the steep density gradients in TBs, but this is not included in this work due to limitations of space. Currently we are investigating the conventional and unconventional TEMs in TBs, and will report the result in the near future.

3.5. Magnetic shear $\hat{s}$ effects

In this section, we study the effect of magnetic shear on the ITG modes with different mode-numbers at steep gradients and compare with the results of conventional ITG modes in the L-regime of medium gradients. It is noted that the growth rate and real frequency in the cases of steep and medium gradients are normalized to electron diamagnetic drift frequencies ω_{*e1} and ω_{*e2} respectively, because ω_{*e1} and ω_{*e2} depend on the value of L_n. The conventional ITG mode in the L-regime has the maximum growth rate at $k_\theta\rho_s = 0.6$, as shown in figure 3(*c*); thus, the case of $k_\theta\rho_s = 0.6$ is taken. It is shown in figure 8(*a*) that with increasing $\hat{s}$ at steep gradients, the ITG modes with $l = 0$–5 are strongly destabilized in the weak positive magnetic shear region and then slightly stabilized—which is different from the case at medium gradients, where the conventional mode is always stabilized (shown by the purple dashed line with solid circles). It is noticeable in figure 8(*b*) that with increasing $\hat{s}$, the normalized real frequency of the ITG modes with $l = 0$–5 at steep gradients decreases faster than that of the conventional mode at medium gradients.

From the gyrokinetic equation (3), we get the local ($k_{//} =$ constant) electrostatic response of ions $f_i = -\frac{eF_M}{T_i}\widehat{\phi}(\theta) +$

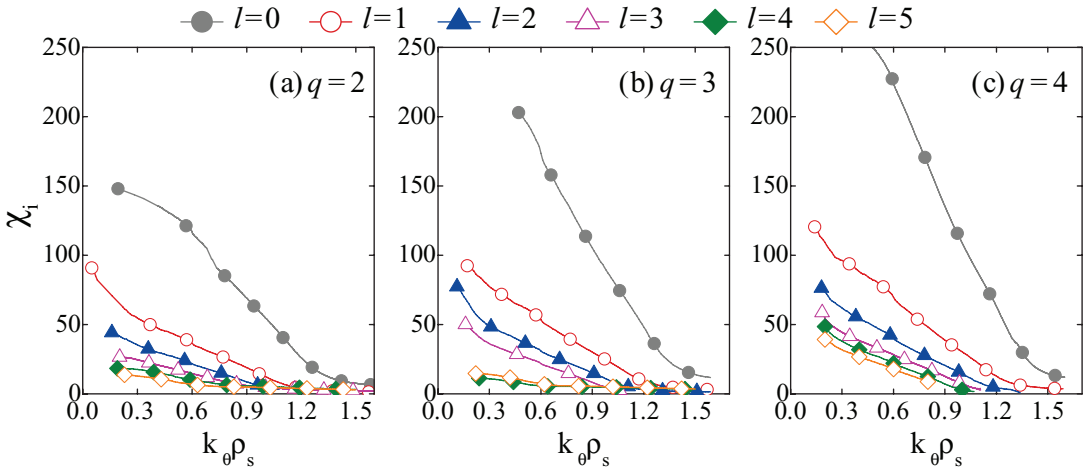

Figure 9. Radial transport coefficient estimated with mixing length approximation for ITG modes with $l = 0$–5 versus $k_\theta\rho_s$. (*a*), (*b*) and (*c*) are for $q = 2, 3, 4$ respectively. The other parameters are the same as those in figure 1.

$\frac{eF_M}{T_i}\left(\frac{\omega-\omega_{*T}}{\omega-\omega_D-k_{//}v_{//}}\right)J_0^2(\alpha_i)\widehat{\phi}(\theta)$ [30]. Thus, the ion Landau resonance/damping mechanism works at $\omega \sim \omega_D + k_{//}v_{//}$. Figure 8 shows that the real frequencies of the modes at steep or medium gradients increase with increasing magnetic shear. It is also shown in figure 8 that the conventional ITG mode (the dashed purple line with solid circle) is evidently stabilized with the increase of the magnetic shear. This is due to the real frequencies $\omega \sim \omega_D + k_{//}v_{//}$ ($-2.2 < \omega/\omega_{*e2} < -1.8$). Hence, it is the ion Landau damping that mainly takes place, since ω_{*e2} is low. As shown in figure 8, the modes at steep gradients are first destabilized and then slightly stabilized, because their real frequencies are very high $\omega \gg \omega_D + k_{//}v_{//}$ ($-0.1 < \omega/\omega_{*e1} < -0.8$) and ω_{*e1} is very high. Therefore, the Landau damping is weak.

Interestingly, the unstable eigenmodes with higher mode-number $l \geqslant 6$ are also excited. The value of the magnetic shear, which induces a peak in the mode growth rate, increases with increasing mode-number l. These results are not listed in this work. In addition, it is noted that the effects of magnetic shear on unconventional ITG modes at steep gradients are similar to those on the short wavelength ion temperature gradient (SWITG) modes ($k_\theta\rho_s \gg 1$) [33, 38, 39]. Hirose *et al* observed that the increase of magnetic shear always destabilizes the SWITG modes in the positive magnetic shear region, when the medium density gradient ($\varepsilon_n = 0.1$) and steep ITG ($\varepsilon_{Ti} = 0.04$) are considered [39].

3.6. Radial mixing length estimation

Under conditions in which anomalous transport driven by drift instabilities dominates, it is found that a model for particle transport can describe the density profiles measured in L-mode and H-mode, observed on some devices [40–43].

To examine the radial turbulent transport driven by ITG instabilities in tokamaks roughly, the quasi-linear mixing length estimation of the diffusion coefficient of unconventional modes,

$$\chi_i = \frac{\widehat{\gamma}}{\widehat{k}_r^2}\frac{k_\theta\rho_s}{\varepsilon_n}\left(\frac{c_s}{R}\rho_s^2\right), \tag{18}$$

with

$$\widehat{k}_r^2 = k_\theta^2\rho_s^2\hat{s}^2\langle\theta^2\rangle, \tag{19}$$

is obtained, based on the gyrokinetic treatment. Here, $\widehat{k}_r$ represents the average of normalized radial wave number, employing the $s-\alpha$ geometry with $\alpha = 0$ which was first used by Kadomtsev [44]. It must be stressed that growth rate $\widehat{\gamma}$ in equation (18) is normalized to ω_{*e} and transport coefficients χ_i in figures 9–11 are normalized to $\frac{c_s}{R}\rho_s^2$.

The radial transport coefficients estimated with mixing length approximation for ITG modes with $l = 0$–5 versus $k_\theta\rho_s$ are given in figures 9(*a*)–(*c*) for $q = 2.0$, 3.0, 4.0, respectively. The other parameters are the same as those in figure 1. It is easy to observe that at steep gradients, the transport coefficients induced by the modes with $l = 0$–5 decrease with increasing normalized poloidal wave number $k_\theta\rho_s$. Evidently, the sum of the transport coefficients induced by the modes with $l \neq 0$ is larger than that of mode $l = 0$ in small and medium $k_\theta\rho_s$ regions. This observation demonstrates that the contribution of modes with $l \neq 0$ to transport indeed deserves more attention. Figures 9(*a*)–(*c*) also illustrate that for a monotonic q profile, the increase of q value leads to an increase of mixing length estimated transport.

In previous sections, moreover, the individual effect of ion temperature and density gradients on the growth rate is studied systemically. Correspondingly, their contributions to the radial transport are investigated individually here. The radial transport coefficients estimated with mixing length approximation for ITG modes with $l = 0$–5 versus ε_{Ti} are given in figure 10 for $k_\theta\rho_s = 0.55$, 0.65, 0.9. The other parameters are the same as those in figure 5. It is clearly indicated that, as expected, increasing the ITG (reducing ε_{Ti}) enlarges the value of radial mixing length transport. Moreover, it is notably observed that the sum of radial transport of modes with $l \neq 0$ is larger than that of the $l = 0$ mode for a very steep temperature gradient ($\varepsilon_{Ti} < 0.02$), and comparable to that of the $l = 0$ mode for a normal temperature gradient ($\varepsilon_{Ti} > 0.02$). On the other hand, the radial transport decreases with increasing $k_\theta\rho_s$, similarly to the result shown in figure 9.

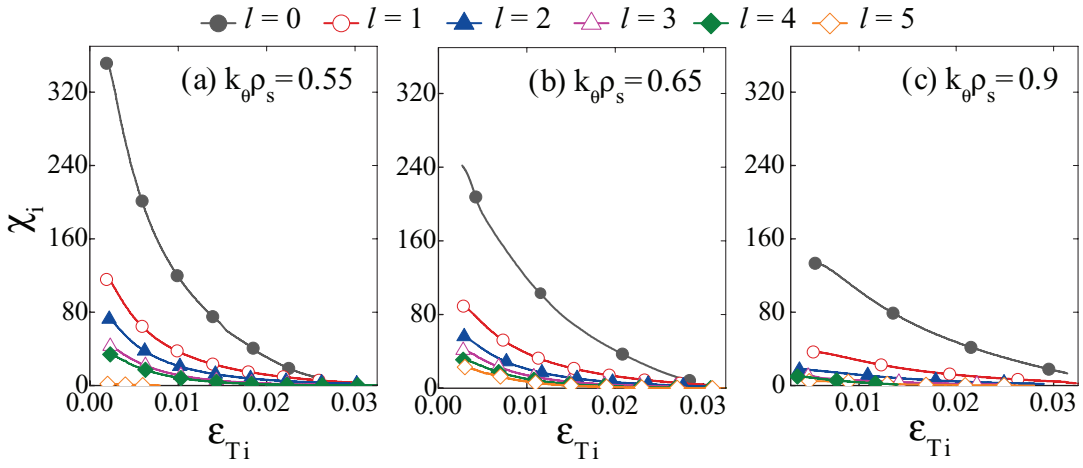

Figure 10. Radial transport coefficient estimated with mixing length approximation for ITG modes with $l = 0$–5 versus ε_{Ti}. The other parameters are the same as those in figure 5.

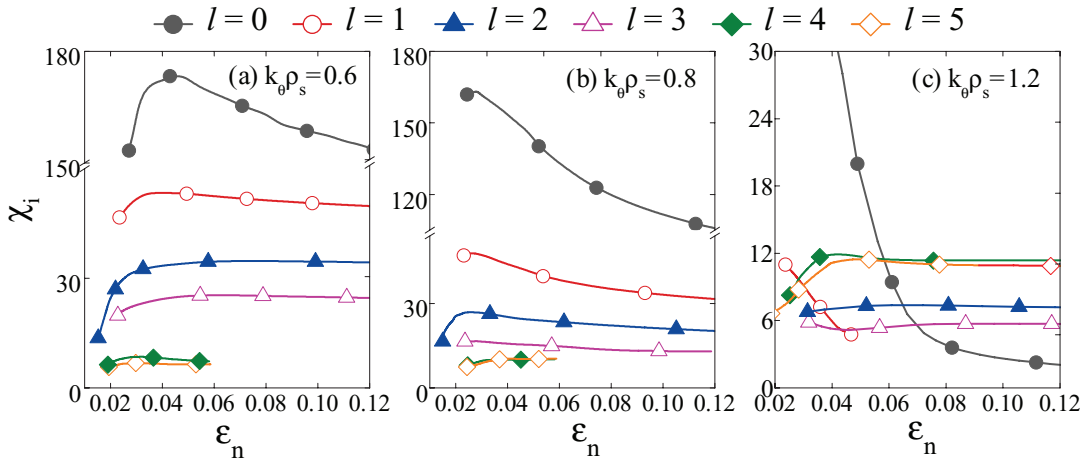

Figure 11. Radial transport coefficient estimated with mixing length approximation for ITG modes with $l = 0$–5 versus ε_n. The other parameters are the same as those in figure 7.

Finally, the radial transport coefficients estimated with mixing length approximation for ITG modes with $l = 0$–5 versus ε_n are given in figure 11 for $k_\theta\rho_s = 0.6$, 0.8, 1.2. The other parameters are the same as those in figure 7. The growth rates are also normalized to $3\varepsilon_n\omega_{*e}/\gamma k_\theta\rho_s$. It is shown that although the radial mixing length transport of the $l = 0$ mode is dominant for $k_\theta\rho_s = 0.6$, 0.8, those of the $l = 4$, 5 modes gradually become dominant with increasing ε_n for $k_\theta\rho_s = 1.2$, as shown in figure 11(*c*).

4. Conclusion and discussion

In this paper, we have presented numerical results on multiple ITG modes in TBs of tokamaks, using the toroidal gyrokinetic eigenvalue code HD7. Both symmetric (the even-parity and the odd-parity) and asymmetric solutions were obtained numerically with the upgraded HD7 code. The full ion kinetics, including the ion toroidal drift, transit motion, and full finite ion Larmor radius effects were taken into account. The ballooning representation was employed so that the linear mode coupling due to the toroidal magnetic configuration was taken into account.

The characteristics of conventional and unconventional ITG modes at steep ion temperature and density gradients have been investigated in detail and compared with the conventional ITG modes at small or medium ion temperature and density gradients. The main results of this work can be summarized as follows.

(1) Multiple ITG modes with conventional and unconventional ballooning mode structures are found unstable simultaneously in TBs with steep density and ITGs—which is different from the case with low or medium gradients, where only one mode with conventional ballooning mode structure is unstable.

(2) At steep ion temperature and density gradients in TBs, the unconventional modes ($l \neq 0$) are dominant in the small $k_\theta\rho_s$ region ($k_\theta\rho_s < 0.4$), conventional mode ($l = 0$) dominates in the medium $k_\theta\rho_s$ region ($0.4 \leqslant k_\theta\rho_s < 1.2$) and the unconventional modes with large mode-number ($l \geqslant 4$) are dominant in the large $k_\theta\rho_s$ region ($k_\theta\rho_s \geqslant 1.2$). These different domination regimes can help to account for the observations of the ‘frequency jump’ and ‘eigenstate jump’ in some simulations obtained using initial-value codes.

(3) The widths of the modes with small mode-numbers in ballooning space first decrease and then increase with increasing $k_\theta\rho_s$, while those with large mode-numbers decrease with increasing $k_\theta\rho_s$ across the whole $k_\theta\rho_s$ region, and even are lower than those of the modes with small mode-number in the large $k_\theta\rho_s$ region. Moreover, the widths of the eigenfunctions of conventional and unconventional modes broaden in k space with the increase of $k_\theta\rho_s$.

(4) When the individual roles of ITG $\varepsilon_{T\mathrm{i}}$ and density gradient ε_n are studied separately, the results indicate that it is the synergetic effect of $\varepsilon_{T\mathrm{i}}$ and ε_n rather than $\varepsilon_{T\mathrm{i}}$ alone that drives the unconventional ITG modes with large mode-number in TBs. The critical value of ε_n for driving such modes with large mode-number increases with increasing $k_\theta\rho_s$.

(5) The magnetic shear $\hat{s}$ first strongly destabilizes the unconventional ITG modes in the weak positive magnetic shear region, and then slightly stabilizes them in the large positive magnetic shear region as $\hat{s}$ increases. The tendency in the large $\hat{s}$ region is different from the case of the conventional ITG modes at medium gradients, where the magnetic shear significantly stabilizes the mode.

(6) The sum of the radial turbulent transport estimated with mixing length approximation from the modes with $l \neq 0$ is larger than that from the mode $l = 0$, and the radial mixing length transport of the $l = 4$, 5 modes are dominant for $k_\theta\rho_s = 1.2$.

From the unstable spectra, eigenmode structures and mixing length transport presented in this work, it is demonstrated that the multiple unstable ITG modes exist and, in particular, the unconventional ITG modes inevitably play significantly important roles in the turbulent transport in TBs of tokamaks. Hence a complete understanding of the characteristics of such modes is urgently needed for the further exploration of the transition of confinement regimes and transport in TBs. It is worthwhile to mention that a finite equilibrium ion parallel velocity and ion parallel velocity shear, as well as up/down asymmetries in the flux surface geometry, can break mode parity and may change which mode is the most unstable. Nevertheless, studies of the effects of the shear flows and ion parallel velocity shear, as well as trapped electrons and electromagnetic perturbations, on the multiple ITG modes in TBs are in progress. Finally, it has to be pointed out that, although the shear flow effect [45] is not considered in this work, the results obtained in this work still provide the most fundamental insight into the excitation of such ITG modes when the shearing rate of the flow is smaller than the growth rate of the modes.

Acknowledgments

The authors thank Zhe Gao, H.S. Xie, P.H. Diamond, T.S. Hahm, C. Angioni and J. Weiland for valuable and helpful discussions. This work is supported by National Magnetic Confinement Fusion Science Program of China under Grant Nos. 2014GB124000 and 2013GB111000, National Natural Science Foundation of China under Grant Nos. 11322549 and 11675038, and the Fundamental Research Funds for the Central Universities under Grant No. DUT15YQ103.

References

[1] Connor J.W. and Wilson H.R. 1994 *Plasma Phys. Control. Fusion* **36** 719
[2] Brizard A. and Hahm T.S. 2007 *Rev. Mod. Phys.* **79** 421
[3] Kikuchi M. and Azumi M. 2015 *Frontier in Fusion Research II* (Berlin: Springer) ch 5
[4] Weiland J. 2016 *Plasmas Phys. Rep.* **42** 502
[5] Dong J.Q., Horton W. and Kim J.Y. 1992 *Phys. Fluids* B **4** 1867
[6] Li J. Q., Ding H. C. and Huang L. 1996 *Phys. Plasmas* **3** 3337
[7] Wolf R.C. 2002 *Plasma Phys. Control. Fusion* **45** R1
[8] Synakowski E.J. 1998 *Plasma Phys. Control. Fusion* **40** 581
[9] Connor J.W., Fukuda T., Garbet X., Gormezano C., Mukhovatov V., Wakatani M., the ITB Database Group and the ITPA Topical Group on Transport and Internal Barrier Physics 2004 *Nucl. Fusion* **44** R1
[10] Wang Z.X., Li J.Q., Dong J.Q. and Kishimoto Y. 2009 *Phys. Rev. Lett.* **103** 015004
[11] Hubbard A.E. *et al* 2011 *Phys. Plasmas* **18** 056115
[12] Whyte D.G. *et al* 2010 *Nucl. Fusion* **50** 105005
[13] Fulton D., Lin Z., Holod I. and Xiao Y. 2014 *Phys. Plasmas* **21** 042110
[14] Xu G.S. *et al* 2011 *Phys. Rev. Lett.* **107** 125001
[15] Wang E. *et al* 2012 *Nucl. Fusion* **52** 103015
[16] Xu X.Q., Xia T.Y., Liu Z.X., Kong D.F., Diallo A., Groebner R.J., Hubbard A.E. and Hughes J.W. 2016 *Phys. Plasmas* **23** 055901
[17] Xie H. and Xiao Y. 2015 *Phys. Plasmas* **22** 090703
[18] Rafiq T., Anderson J., Nadeem M. and Persson M. 2001 *Plasma Phys. Control. Fusion* **43** 1363
[19] Singh R., Brunner S., Ganesh R. and Jenko F. 2014 *Phys. Plasmas* **21** 032115
[20] Romanelli F. 1989 *Phys. Fluids* B **1** 1018
[21] Xie H. and Li B. 2016 *Phys. Plasmas* **23** 082513
[22] Lu G.M., Shen Y., Xie T., Qi L.Y., He Z.X., He H.D. and Cui S.Y. 2013 *Phys. Plasmas* **20** 102505
[23] Sugama H. 1999 *Phys. Plasmas* **6** 3527
[24] Tang W.M. 1978 *Nucl. Fusion* **18** 1089
[25] Dong J.Q. and Horton W. 1995 *Phys. Plasmas* **2** 3412
[26] Shen Y., Dong J.Q., Sun A.P., Qu H.P., Lu G.M., He Z.X., He H.D. and Wang L.F. 2016 *Plasma Phys. Control. Fusion* **58** 045028
[27] Dong J.Q., Sanuki H. and Itoh K. 2001 *Phys. Plasmas* **8** 8
[28] Dong J.Q. and Horton W. 1993 *Phys. Fluids* B **5** 1581
[29] Dong J.Q., Horton W. and Kishimoto Y. 2001 *Phys. Plasmas* **8** 167
[30] Dong J.Q., Chen L. and Zonca F. 1999 *Nucl. Fusion* **39** 1041
[31] Dong J.Q., Chen L., Zonca F. and Jian G.D. 2004 *Phys. Plasmas* **11** 997
[32] Gao Z., Sanuki H., Itoh K. and Dong J. Q. 2005 *Phys. Plasmas* **12** 022502
[33] Du H., Wang Z.X. and Dong J.Q. 2015 *Phys. Plasmas* **22** 022506
[34] Liu S.F., Guo S.C., Kong W. and Dong J.Q. 2013 *Phys. Plasmas* **20** 032309
[35] Zhong W.L. *et al* 2016 *Phys. Rev. Lett.* **117** 045001
[36] Holod I. and Lin Z. 2013 *Phys. Plasmas* **20** 032309
[37] Guo S.C. and Weiland J. 1997 *Nucl. Fusion* **37** 8
[38] Hirose A. and Elia M. 2002 *Phys. Plasmas* **9** 1659
[39] Smolyakov A.I., Yagi M. and Kishimoto Y. 2002 *Phys. Rev. Lett.* **89** 125005
[40] Baker D.R. *et al* 2000 *Nucl. Fusion* **40** 1003

[41] Angioni C., Peeters A.G., Pereverzev G.V., Ryter F., Tardini G. and ASDEX Upgrade Team 2003 *Phys. Rev. Lett.* **90** 205003
[42] Weisen H. *et al* 2005 *Nucl. Fusion* **45** L1–L4
[43] Takenaga H. *et al* 2008 *Nucl. Fusion* **48** 075004
[44] Kadomtsev B.B. 1965 *Plasma Turbulence* (New York: Academic) ch 8
[45] Diamond P.H., Itoh S., Itoh K. and Hahm T.S. 2005 *Plasma Phys. Control. Fusion* **47** R35